

Numerical Study of Extreme Adverse Pressure Gradients Enabled by Co-Flow Jet

B. McBreen,^{*} K.-W. Xu,[†] G.-C. Zha,[‡]
Dept. of Mechanical and Aerospace Engineering
University of Miami, Coral Gables, Florida 33146
E-mail: gzha@miami.edu

Abstract

This paper conducts a 2D numerical study of flows with extreme adverse pressure gradients (EAPG) enabled by Co-Flow Jet (CFJ) active flow control (AFC). An EAPG is defined to be an adverse pressure gradient of at least one order of magnitude greater than that which could be sustained by the non-controlled flow of a baseline case. The flow field is solved using the Unsteady Reynolds Averaged Navier-Stokes (URANS) equations with the one-equation Spalart-Allmaras turbulence model. A CFJ cylinder and CFJ airfoil with EAPG and attached flow are studied, showing lift coefficients up to 19.68 and 15.96 respectively. The CFJ airfoil maintains attached flow in a maximum streamwise adverse pressure gradient 1091 times greater than the baseline airfoil, and a maximum radial adverse pressure gradient 121 times greater than the baseline airfoil. Similarly, the CFJ cylinder shows attached flow with a streamwise pressure gradient ratio up to 17 and radial pressure gradient ratio up to 132. Such an extraordinary adverse pressure gradient ratios motivate this effort to investigate how the implementation of the CFJ can achieve this effect. Due to its ability to maintain attached flow in the presence of an EAPG, the CFJ offers a highly effective method of active flow control with the potential to be far more effective than other active flow control devices.

Nomenclature

<i>AoA</i>	Angle of Attack, α
<i>AFC</i>	Active Flow Control
<i>APG</i>	Adverse Pressure Gradient
<i>CFJ</i>	Co-Flow Jet
<i>CFWJ</i>	Co-Flow Wall Jet
<i>EAPG</i>	Extreme Adverse Pressure Gradient
<i>FASIP</i>	Flow-Acoustics-Structure Interaction Package
<i>LE</i>	Leading Edge
<i>RANS</i>	Reynolds-Averaged Navier-Stokes
<i>TE</i>	Trailing Edge
<i>ZNMF</i>	Zero-Net Mass Flux
PG_x	Normalized Streamwise Pressure Gradient, $\frac{C}{0.5\rho_\infty V_\infty^2} \frac{\partial p}{\partial x}$
PG_r	Normalized Radial Pressure Gradient, $\frac{C}{0.5\rho_\infty V_\infty^2} \frac{\partial p}{\partial r}$
PGR_x	Streamwise Pressure Gradient Ratio, $PG_x(CFJ)/PG_x(Baseline)$

^{*} Ph.D. Candidate

[†] Ph.D. Candidate.

[‡] Professor, AIAA Associate Fellow

PGR_r	Radial Pressure Gradient Ratio, $PG_r(CFJ)/PG_r(Baseline)$
P	CFJ pumping power consumption, $P = \frac{\dot{m}C_p T_{t2}}{\eta} (\Gamma^{\frac{\gamma-1}{\gamma}} - 1)$
η	CFJ pumping system efficiency, propeller efficiency
P_c	Power coefficient, $P_c = \frac{P}{\frac{1}{2}\rho_\infty V_\infty^3 S}$
PR	Total pressure ratio, Γ
C_L	Lift coefficient
C_D	Drag coefficient
C_μ	Jet momentum coefficient, $C_\mu = \frac{\dot{m}V_j}{\frac{1}{2}\rho_\infty V_\infty^2 S}$
C_{Lmax}	Maximum lift coefficient
$(L/D)_c$	Aerodynamic efficiency corrected for CFJ airfoil, $\frac{L}{D+P/V_\infty}$
Re	Reynolds number
Ma	Mach number
C_p	Pressure coefficient
γ	Air specific heats ratio
ρ_∞	Freestream density
V_∞	Freestream velocity
T_t	Total temperature
P_t	Total pressure
H_t	Total specific enthalpy
\dot{m}	Mass flow across the pump
ω_z	Spanwise Vorticity
C, c	Chord length
r_c	Radius of Curvature
κ	Curvature, $1/r_c$

1 Introduction

Active Flow Control (AFC) may substantially extend the operating limits of a flow system without stall. Consequently, an AFC system may significantly increase pressure gradients within the flow. When the maximum adverse pressure gradient exceeds ten times the maximum gradient observed in a non-controlled flow system, we will refer to it as an extreme adverse pressure gradient (EAPG). Co-Flow Jet (CFJ) active flow control is a technique which has been shown numerically to achieve and sustain an EAPG, reaching extraordinary pressure gradient magnitudes in the systems presented within this paper.

There is a causal relationship between the maximum adverse pressure gradient and flow attachment. As an airfoil rotates to higher angles of attack, the adverse pressure gradient it can sustain on the suction surface increases until the onset of separated flow. The maximum streamwise pressure gradient occurs on the surface immediately upstream of the separation onset location. Once the flow is separated, the pressure gradient is relaxed in the flow separated region. An airfoil cannot have attached flow without an adverse pressure gradient, and a sizeable adverse pressure gradient does not occur with flow separation.

The CFJ airfoil is a zero-net-mass-flux flow control using fluidic actuators developed by Zha and his team [1, 2, 3, 4, 5, 6, 7, 8, 9, 10, 11, 12, 13, 14, 15, 16, 17, 18, 19]. The CFJ airfoil has a tangential injection slot near the leading edge (LE) of the airfoil's top surface and a streamwise suction slot near the trailing edge (TE), shown in Fig. 1. A small amount of the flow over the top surface is ingested into the airfoil through the suction slot, pressurized and energized by a small axial compressor inside the airfoil, then injected near the leading edge

through the injection slot. The CFJ airfoil possesses high control authority due to its fluidic actuators, very high stall AoA (potentially up to 80°), ultra-high lift coefficient, and very low energy expenditure.

Since the co-flow jet has tangential injection and streamwise suction, it is categorized as a wall jet. In this paper, the term “co-flow wall jet” (CFWJ) will specifically refer to the jet flow, while “co-flow jet” (CFJ) will be used when describing the airfoil plus internal pump system. Since jet injection usually destabilizes flow, co-flow wall jets are categorized as turbulent wall jets [16].

Fig. 2 pictures the CFJ-NACA6421 airfoil tested in a subsonic wind tunnel with five micro-compressor actuators embedded inside the airfoil [13, 20]. The drag polar plot Fig. 3 shows a $C_{Lmax} = 8.6$ was achieved in this testing, far greater than the $C_{Lmax} = 1.5$ achieved with the baseline airfoil. This CFJ airfoil also generates a thrust up to $C_D = -1.0$. The CFJ airfoil operates without stall at much higher angles of attack than the baseline airfoil.

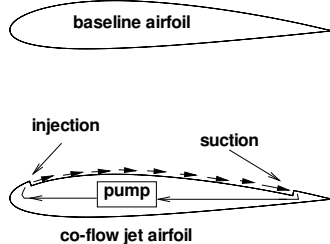


Figure 1: CFJ airfoil concept.

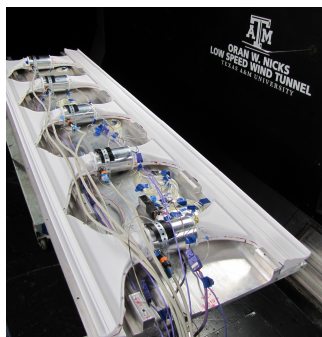


Figure 2: Photo of the wind tunnel tested airfoil with 5 fans embedded.

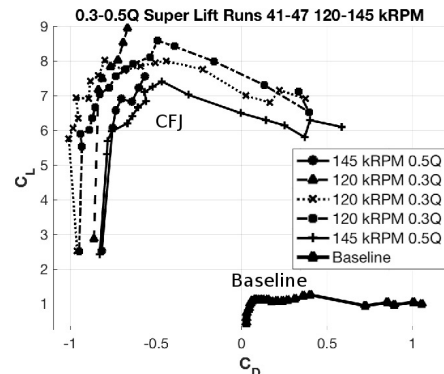


Figure 3: Measured drag polar of the CFJ and baseline airfoil.

The maximum lift coefficient an airfoil can create is governed in part by the maximum adverse pressure gradient (APG) that airfoil can sustain before stalling. Smith [21] gives the following maximum lift coefficient limit, based on potential flow theory and the Kutta condition at an angle of attack of 90° :

$$C_{Lmax} = 2\pi\left(1 + \frac{t}{c}\right) \quad (1)$$

For a cylinder with $t/c = 1$, the C_{Lmax} limit will be 4π and is consistent with Prandtl’s conclusion [22]. However, the cylinder C_{Lmax} limit was exceeded by Lockwood et al. in 1960 [23] using multiple tangential blowing slots on the cylinder surface. They achieved $C_{Lmax} \approx 20$ with a very high injection momentum coefficient of $C_\mu \approx 5$. Tokumaru and Dimotakis in 1993 [24] achieved $C_{Lmax} \approx 14$ by using a rotating cylinder. Based on potential flow theory, the stagnation point should be detached from the cylinder surface when C_{Lmax} is greater than 4π . Neither study investigated the flow structures. A maximum lift coefficient that exceeds the C_{Lmax} defined in Eq. (1) is termed a “super-lift coefficient” [12].

Yang and Zha [25] applied CFJ flow control to a cylinder using 2D Reynolds Averaged Navier-Stokes (RANS) simulation with the one-equation Spalart-Allmaras turbulence model [26], achieving a C_{Lmax} of 28 at $C_\mu=0.8$ in their study, far exceeding $C_{Lmax} = 4\pi$ dictated by Eq. (1). They further applied CFJ to the CFJ-NACA6421 airfoil at a free-stream Mach number of 0.063 [12]. While Yang and Zha identified SLC conditions for their CFJ airfoil and cylinder studies, they did not identify or quantify the EAPG and its contribution to the SLC. This paper analyzes the magnitude of the EAPG and its contribution to creating a SLC for CFJ airfoils and CFJ cylinders.

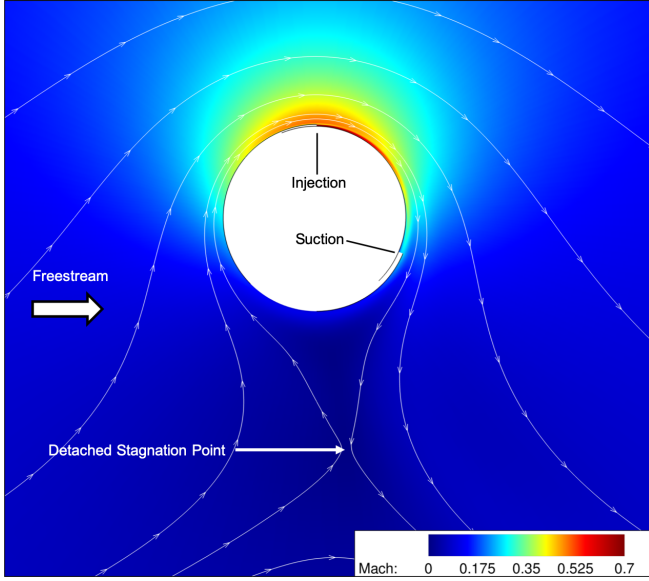


Figure 4: CFJ cylinder Mach contours and streamlines at $C_\mu = 0.7$.

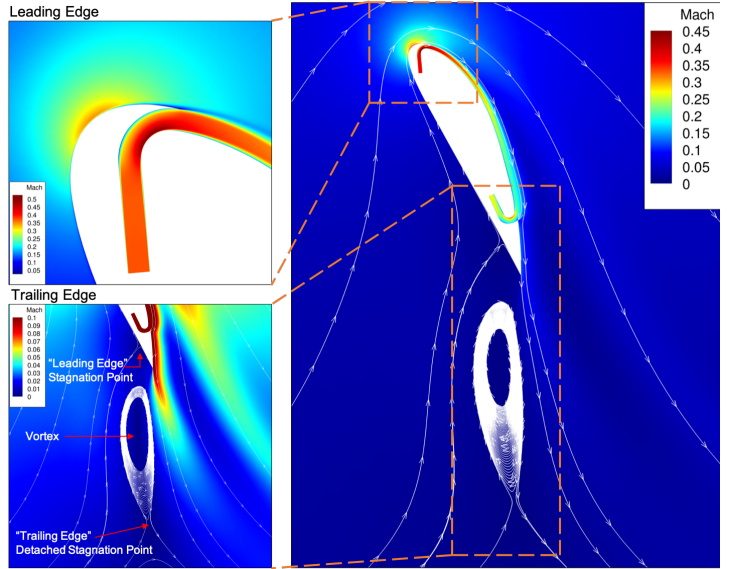


Figure 5: CFJ airfoil Mach contours and streamlines at $C_\mu = 4.5$ and $AoA = 65^\circ$ for the CFJ6421 airfoil.

The pressure gradient coefficient in the streamwise and centrifugal direction are defined as:

$$PG_x = \frac{C}{0.5\rho_\infty V_\infty^2} \frac{\partial p}{\partial x}, \quad PG_r = \frac{C}{0.5\rho_\infty V_\infty^2} \frac{\partial p}{\partial r} \approx \frac{C}{0.5\rho_\infty V_\infty^2} \frac{\rho V_t^2}{R} \quad (2)$$

where the subscript x denotes the streamwise direction, r denotes the radial direction transverse to the flow, C is the airfoil chord, V_t is the tangential velocity, and R is the local curvature radius. For the purposes of this paper, we define an EAPG to be a pressure gradient of a value that is at least one order of magnitude greater than the maximum pressure gradient from the flow field of a baseline configuration with no flow control and without stall.

Fig. 4 shows example Mach contours with streamlines for the CFJ cylinder studied in this paper. This CFJ cylinder positions the injection slot at the 12 o'clock position and the suction slot clockwise 112.5° from the injection slot. The CFJ completely removes the flow separation caused by vortex shedding behind the cylinder. The stagnation point is shown to be detached from the solid surface, in line with predictions from potential flow theory.

Fig. 5 shows that the studied CFJ-NACA6421 airfoil had attached flow at AoA of 65° and $C_\mu = 4.5$ with a $C_L = 15.96$, which exceeds the potential flow limit of 7.6. The circulation is so high that the stagnation point detaches from the airfoil sharp trailing edge, shown in Fig. 5. The trailing edge vortex creates a lifting effect approximately equivalent to an extension of the airfoil solid body to the stagnation point.

The stagnation point detachment from a sharp airfoil trailing edge does not appear to be documented in fluid mechanics literature and contradicts the Kutta condition from classical fluid mechanics. Yang and Zha [12] argue that it does not violate flow physics, remarking that the Kutta condition is a conceptual mathematical condition to enforce a unique solution of potential airfoil flows. It is not a physical condition that real flows or Navier-Stokes equations must always satisfy. The Kutta condition is valid for a subset of airfoil solutions, which have prescribed circulations with the stagnation points located at the leading and trailing edges. When the circulation exceeds the limit, the trailing edge stagnation point can detach in the same manner as the CFJ cylinder, and the lift coefficient will continue to increase.

This paper numerically examines flow with an EAPG which is enabled by the implementation of the CFJ. Understanding the flow physics is important for optimal design of fluid systems with CFJ. Xu et al [16] analyze the mechanism of CFJ separation control with adverse pressure gradient (APG), which uses the NASA hump as the study case. However, the APG of the NASA hump is mild and is not an EAPG. This paper provides the numerical observation as the basis for further investigation of the EAPG mechanism.

1.1 CFWJ Flow Profile

Launer and Rodi [27] define a wall jet as a “boundary layer in which, by virtue of the initially supplied momentum, the velocity over some region in the shear layer exceeds that in the free stream” as illustrated in Fig. 6, a). A wall jet can be viewed as having two shear layers: 1) the inner layer similar to conventional turbulent boundary layer; 2) the outer layer that is more like a free shear layer. Launer and Rodi indicate that the essential difference of a wall jet from conventional boundary layer is that the shear stress of the inner layer and outer layer have opposite sign and the maximum shear stress of the outer layer is usually several times larger than the wall shear stress. This means that the inner and outer layer have opposite spanwise vorticity sign or counter rotating vortices. A turbulent wall jet always has a strong interaction between the two layers, which results in a shift of the zero shear stress position from the position of maximum velocity (where it would occur for a laminar wall jet) to a position slightly closer to the wall [27, 28, 29, 30].

The sketch Fig. 6 shows the wall velocity profiles created by the CFWJ injection and suction effects. Part a) shows that the injection of CFWJ has a typical wall jet velocity profile with three counter rotating vortex layers: 1) clockwise boundary layer vortex sheet on the wall surface; 2) counter clockwise CFWJ vortex layer due to the high momentum co-flow wall jet injection; 3) the second clockwise vortex layer due to the wake mixing layer. Establishing the wall surface clockwise vorticity is necessary to guarantee attached flow. The stronger the injection jet, the greater the vorticity. Part b) shows the streamwise suction of CFWJ. The CFWJ suction is located downstream to “pull” the flow in the streamwise direction. It also further enhances the clockwise vorticity along the wall. The CFWJ suction draws flow in tangential to the surface, as opposed to other widely used suction flow controls that draw the flow into the wall perpendicularly. It is consequently termed streamwise suction.

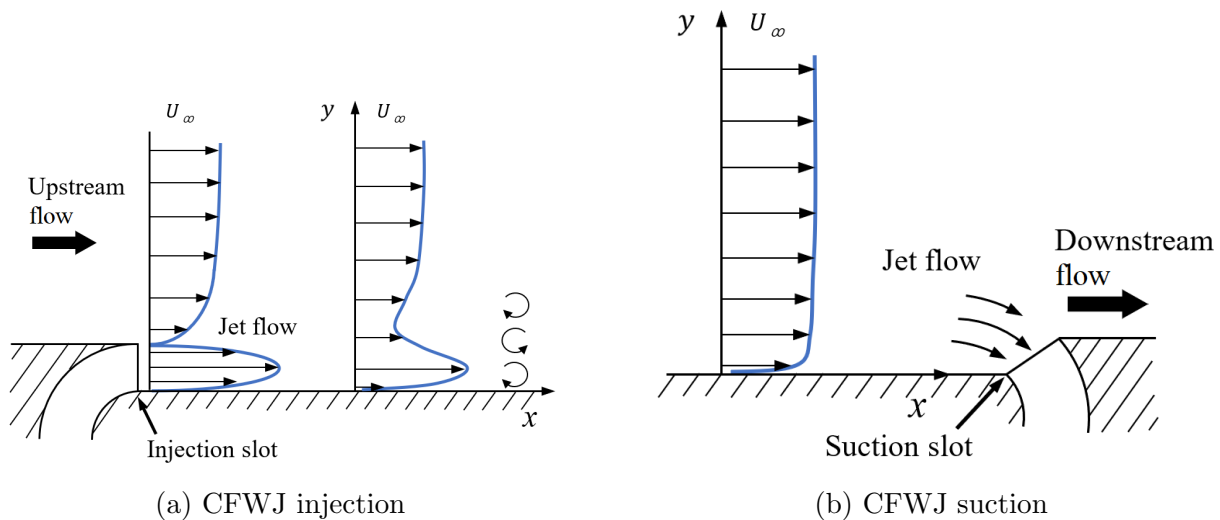


Figure 6: Sketches of CFWJ injection and suction wall velocity profiles.

2 Numerical Methodology

2.1 Governing Equations

The governing equations for the CFD simulation are the 2D Unsteady Reynolds Averaged Navier-Stokes (URANS) equations, with the one equation Spalart-Allmaras turbulence model [26], solved in a fully coupled manner using an implicit unfactored Gauss-Seidel line iteration. The normalized 2D Navier-Stokes governing equations in generalized coordinates are given by:

$$\frac{\partial \mathbf{Q}}{\partial t} + \frac{\partial \mathbf{E}}{\partial \xi} + \frac{\partial \mathbf{F}}{\partial \eta} = \frac{1}{Re} \left[\frac{\partial \mathbf{R}}{\partial \xi} + \frac{\partial \mathbf{S}}{\partial \eta} \right] + \mathbf{S}_\nu \quad (3)$$

The conservative variable vector \mathbf{Q} , inviscid flux \mathbf{E} , viscous flux vector \mathbf{R} are expressed as follows, and the rest can be obtained following the symmetric rule.

$$\mathbf{Q} = \frac{1}{J} \begin{bmatrix} \rho \\ \rho u \\ \rho v \\ \rho e \\ \rho \hat{\nu} \end{bmatrix}, \mathbf{E} = \frac{1}{J} \begin{bmatrix} \rho U \\ \rho u U + p \xi_x \\ \rho v U + p \xi_y \\ (\rho e + p) U \\ \rho \hat{\nu} U \end{bmatrix}, \mathbf{R} = \frac{1}{J} \begin{bmatrix} 0 \\ \tau_{xi} \xi_i \\ \tau_{yi} \xi_i \\ (u_j \tau_{ij} - q_i) \xi_i \\ \frac{\rho}{\sigma} (\nu + \hat{\nu}) \frac{\partial \hat{\nu}}{\partial x_i} \xi_i \end{bmatrix}, \mathbf{S}_\nu = \begin{bmatrix} 0 \\ 0 \\ 0 \\ 0 \\ S_\nu \end{bmatrix}$$

The \mathbf{S}_ν in Eq. (3) is the source term for the S-A model,

$$S_\nu = \frac{1}{J} \left[\frac{1}{Re} \left[-\rho (c_{w1} f_w - \frac{c_{b1}}{\kappa^2} f_{t2}) (\frac{\tilde{\nu}}{d})^2 \right] + \frac{1}{Re} \left[\frac{\rho}{\sigma} c_{b2} (\nabla \tilde{\nu})^2 - \frac{1}{\sigma} (\nu + \tilde{\nu}) \nabla \tilde{\nu} \bullet \nabla \rho \right] + Re \left[\rho f_{t1} (\Delta q)^2 \right] + \rho c_{b1} (1 - f_{t2}) \tilde{S} \tilde{\nu} \right] \quad (4)$$

Other auxiliary relations and coefficients for the S-A turbulence model can be found in [26, 31].

2.2 Boundary Conditions

Freestream conditions including total pressure, total temperature, and flow angle are specified for the upstream portion of the far field boundary. For far field downstream boundary, the static pressure is specified as freestream value to match the intended freestream Mach number. The wall treatment suggested in [32] to achieve flux conservation by shifting half interval of the mesh on the wall is employed. If the wall surface normal direction is in η -direction, the no slip condition is enforced on the surface by computing the wall inviscid flux $F_{1/2}$ in the following manner:

$$\mathbf{F}_w = \begin{pmatrix} \rho V \\ \rho u V + p \eta_x \\ \rho v V + p \eta_y \\ \rho w V + p \eta_z \\ (\rho e + p) V \end{pmatrix}_w = \begin{pmatrix} 0 \\ p \eta_x \\ p \eta_y \\ p \eta_z \\ 0 \end{pmatrix}_w \quad (5)$$

2.3 CFD Solver

The in-house high order CFD code Flow-Acoustics-Structure Interaction Package (FASIP) is used to solve the 2D Unsteady-Reynolds Averaged Navier-Stokes equations with the one-equation Spalart-Allmaras turbulence model [26]. A 5th order WENO scheme [33, 32, 34, 31] for the inviscid flux and a 2nd order central differencing for the viscous terms [35, 36] are employed to discretize the Navier-Stokes equations. The low diffusion E-CUSP scheme based on the Zha-Bilgen flux vector splitting [37] is utilized with the WENO scheme to evaluate the inviscid fluxes. All the simulations in this study are conducted as unsteady time accurate simulations. The second order time-accurate implicit time marching method with pseudo time and Gauss-Seidel line relaxation is used to achieve a fast convergence rate [38]. Parallel computing is implemented to save simulation time [39]. The FASIP code has been intensively validated for CFJ simulations. The numerical results are presented after the flows and aerodynamic forces are dynamically stable.

2.4 Co-Flow Jet Parameters

2.4.1 Lift and Drag Calculation

The momentum and pressure at the injection and suction slots produce a reactionary force not included in the surface integral used to calculate lift and drag on the airfoil surface. Using control volume analysis, the reactionary force can be calculated using the flow parameters at the injection and suction slot opening surfaces. Zha et al. [1] give the following formulations to calculate the lift and drag due to the jet reactionary force for a CFD simulation. By considering the effects of injection and suction jets on the CFJ airfoil, the expressions for these reactionary forces are given as:

$$F_{x_{cfj}} = (\dot{m}_j V_{j1} + p_{j1} A_{j1}) * \cos(\theta_1 - \alpha) - (\dot{m}_j V_{j2} + p_{j2} A_{j2}) * \cos(\theta_2 + \alpha) \quad (6)$$

$$F_{y_{cfj}} = (\dot{m}_{j1} V_{j1} + p_{j1} A_{j1}) * \sin(\theta_1 - \alpha) + (\dot{m}_{j2} V_{j2} + p_{j2} A_{j2}) * \sin(\theta_2 + \alpha) \quad (7)$$

where the subscripts 1 and 2 stand for the injection and suction respectively, and θ_1 and θ_2 are the angles between the injection and suction slot surfaces and a line normal to the airfoil chord. α is the angle of attack.

The total lift and drag on the airfoil can then be expressed as:

$$D = R'_x - F_{x_{cfj}} \quad (8)$$

$$L = R'_y - F_{y_{cfj}} \quad (9)$$

where R'_x and R'_y are the surface integral of pressure and shear stress in x (drag) and y (lift) direction excluding the internal ducts of injection and suction. For the CFD simulation, the total lift and drag are calculated using Eqs. (8) and (9).

2.4.2 CFJ Aerodynamic Efficiency

The conventional airfoil aerodynamic efficiency is defined as $\frac{L}{D}$. However since CFJ active flow control consumes energy, the CFJ corrected aerodynamic efficiency is modified to take into account the energy consumption of the

pump. The formulation of the corrected aerodynamic efficiency for CFJ airfoils is :

$$\left(\frac{L}{D}\right)_c = \frac{L}{D + \frac{P}{V_\infty}} = \frac{C_L}{C_D + P_C} \quad (10)$$

where V_∞ is the free stream velocity, P is the CFJ pumping power, and L and D are the lift and drag generated by the CFJ airfoil. This formulation converts the power consumed by the CFJ into the drag of the airfoil.

2.4.3 CFJ Power Coefficient

The CFJ can be implemented via a pumping system inside the wing that withdraws air from the suction slot and blows it into the injection slot. As a Zero-Net-Mass-Flux (ZNMF) flow control mechanism with a closed flow path, the CFJ power required can be defined by thermodynamic relationship between the mass flow rate and total enthalpy variation. The power consumption can be determined by the jet mass flow and total enthalpy change as the following:

$$P = \dot{m}(H_{t1} - H_{t2}) \quad (11)$$

where H_{t1} and H_{t2} are the total enthalpy in the injection cavity and suction cavity respectively, P is the power required by the pump and \dot{m} the jet mass flow rate. Introducing the pumping efficiency η and total pressure ratio of the pump $\Gamma = \frac{P_{t1}}{P_{t2}}$, the power consumption can be expressed as :

$$P = \frac{\dot{m}C_p T_{t2}}{\eta} (\Gamma^{\frac{\gamma-1}{\gamma}} - 1) \quad (12)$$

The power consumption can be expressed as a power coefficient below:

$$P_c = \frac{P}{\frac{1}{2}\rho_\infty V_\infty^3 S} \quad (13)$$

In this research, the CFJ pumping efficiency is set to 100%. Eq. (12) indicates that the power required by the CFJ is determined linearly by the mass flow rate and exponentially by the total pressure ratio. Large injection slots reduce the power required because the total pressure loss is substantially reduced. It follows that the most efficient way to implement the CFWJ is to employ a large mass flow rate and low total pressure ratio.

2.4.4 Jet Momentum Coefficient

The jet momentum coefficient C_μ is a parameter used to quantify the injection intensity. It is defined as :

$$C_\mu = \frac{\dot{m}V_j}{\frac{1}{2}\rho_\infty V_\infty^2 S} \quad (14)$$

where \dot{m} is the injection mass flow, V_j the injection velocity, ρ_∞ and V_∞ denote the free stream density and velocity, and S is the platform area.

To achieve zero net mass flux with the CFJ flow control, the mass flow exiting the injection slot must be equal to the mass flow entering the suction slot, i.e. $\dot{m}_{inj} = \dot{m}_{suc}$. The prescribed jet momentum coefficient C_μ is achieved by adjusting the injection cavity total pressure. Total temperature is assumed constant during this process. The injection and suction mass flow rates are matched by adjusting the suction cavity static pressure. The iterative process is conducted throughout the simulation until the specified momentum coefficient is reached and the injection and suction mass flow match within the acceptable tolerance, which is 0.5% for the present study.

3 Co-Flow Jet Cylinder

The CFJ cylinder simulations are conducted with freestream Mach number of 0.1 and Reynolds number of 2.4×10^6 . A geometry trade study was conducted to maximize lift while maintaining a subsonic injection flow, in order to curb the power coefficient. The CFJ flow control is implemented by adding injection and suction slots at two streamwise locations on the cylinder surface. The injection slot has a width 1% chord vertically above the center of the cylinder, at the 12 o'clock position, and the suction slot has a width 2.5% chord located 112.5° clockwise from the injection slot. The surface between the slots is translated radially inwards to a varying degree proportional to the slot heights. This translation region is necessary for streamwise injection and suction flows. A small amount of mass flow is ingested into the trailing edge slot, pressurized and energized by a micro-compressor inside the cylinder, then ejected through the injection slot tangential to the main flow.

3.1 Mesh and Boundary Conditions

The computational domain for the 2D cylinder is normalized by the cylinder diameter. A small mesh of 93,000 cells is divided into 12 domains as shown in Fig. 7, left. The boundary conditions are illustrated in Fig. 7, right. The far-field inlet and outlet are located 85 diameters away from the cylinder surface. The total pressure, total temperature, and flow angle are specified at the inlet boundary. Static pressure is specified at the outlet boundary. A non-slip wall BC is enforced on the walls of the cylinder and internal ducts. The pumping of the internal compressor is imitated by applying a total pressure inlet BC at beginning of the injection slot and a static pressure outlet BC at the end of the suction slot. Iteration of the suction static pressure is conducted to match the suction mass flow rate to that of the injection within a tolerance of 1%. Simultaneously, iteration of the injection total pressure is conducted to match the injection C_μ to the target C_μ within a tolerance of 1%. This treatment of the injection and suction is thoroughly validated in previous work [3, 6, 9, 10, 8, 12].

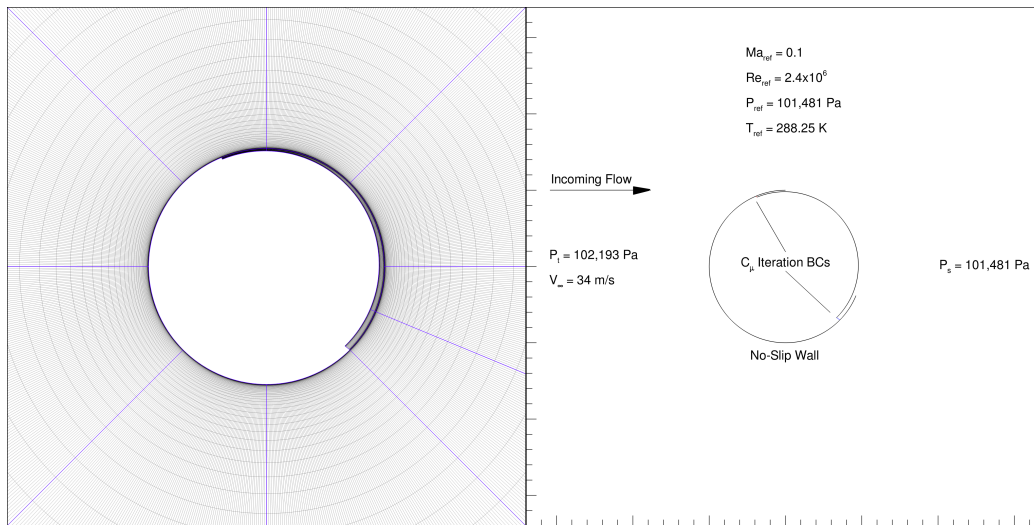


Figure 7: *CFJ cylinder mesh (left), boundary conditions (right).*

3.2 Flow Field

Flow fields for the CFJ cylinder with C_μ higher than 0.85 possess a supersonic injection flow and excessively high P_c . Flow field solutions of the CFJ cylinder show well-attached flow for $C_\mu > 0.45$. Fig. 8 displays a qualitative comparison of the flow fields below the CFJ cylinder for increasing jet momentum coefficients. As C_μ is increased, the LE and TE stagnation points move towards each other on the pressure surface of the cylinder, until just before they meet. This behavior is indicative of the circulation being added to the flow by the CFWJ. Once $C_\mu = 0.45$, the TE stagnation point detaches from the surface of the cylinder, while the LE stagnation point remains at the bottom-most point of the cylinder. In Table 1, the ‘‘Stag. y’’ column identifies the vertical distance of the detached stagnation point from the center of the cylinder. For CFJ cylinder cases with $C_L \geq 13.99$, at least one stagnation point has detached from the surface. At $C_L \geq 15.77$, both LE and TE stagnation points are detached, and merge into a single stagnation point. This stagnation point can be identified in the flow fields by the topological saddle formed by the streamlines below the cylinder.

Table 1: Performance of CFJ cylinder at varying C_μ

C_μ	C_L	C_D	P_c	Γ	C_L/C_D	C_L/C_{Dc}	C_L/P_c	Inj Ma	Stag. y
0.30	9.737	0.149	0.380	1.072	65.349	18.384	25.599	0.504	Attached
0.35	11.098	0.180	0.394	1.070	61.656	19.357	28.197	0.548	Attached
0.40	12.570	0.213	0.467	1.078	59.014	18.486	26.892	0.597	Attached
0.45	13.989	0.248	0.565	1.089	56.407	17.188	24.741	0.647	-0.809
0.50	15.163	0.280	0.675	1.102	54.154	15.871	22.456	0.691	-0.983
0.55	15.767	0.290	0.796	1.115	54.369	14.516	19.804	0.731	-0.942
0.60	16.759	0.317	0.939	1.131	52.868	13.346	17.854	0.775	-1.075
0.65	17.545	0.336	1.089	1.147	52.217	12.310	16.109	0.815	-1.164
0.70	18.196	0.351	1.252	1.164	51.840	11.349	14.535	0.853	-1.232
0.75	18.701	0.363	1.415	1.180	51.518	10.517	13.215	0.886	-1.280
0.80	19.219	0.373	1.616	1.201	51.525	9.663	11.890	0.919	-1.325
0.85	19.684	0.380	1.819	1.221	51.800	8.951	10.823	0.947	-1.367

Once the jet momentum coefficient C_μ reaches 0.55, the LE stagnation point also detaches from the bottom of the cylinder and merges with the TE stagnation point, forming a single unified stagnation point. The flow close to the cylinder circulates uninterrupted within the bounds of the homoclinic orbit. Away from the surface, the upstream incoming flow follows the contour of cylinder, turns around the top of the cylinder by 180° , and continues horizontally. Due to the CFWJ flow mixing which energizes the boundary layer, the flow field is fully attached to the cylinder surface along the entire circumference, as shown in Fig. 4.

Those cylinders possessing a C_μ of 0.45 and higher demonstrate a C_L exceeding Smith’s theoretical limit of 4π , from Eq. (1). It is the cases demonstrating a super-lift coefficient which show a detached stagnation point below the cylinder, consistent with [25]. As the jet momentum coefficient C_μ increases, so does C_L . The stagnation point moves away from the surface of the cylinder roughly directly proportionally to the increasing C_L , at a cost of an increasing P_c , as shown in Fig. 9.

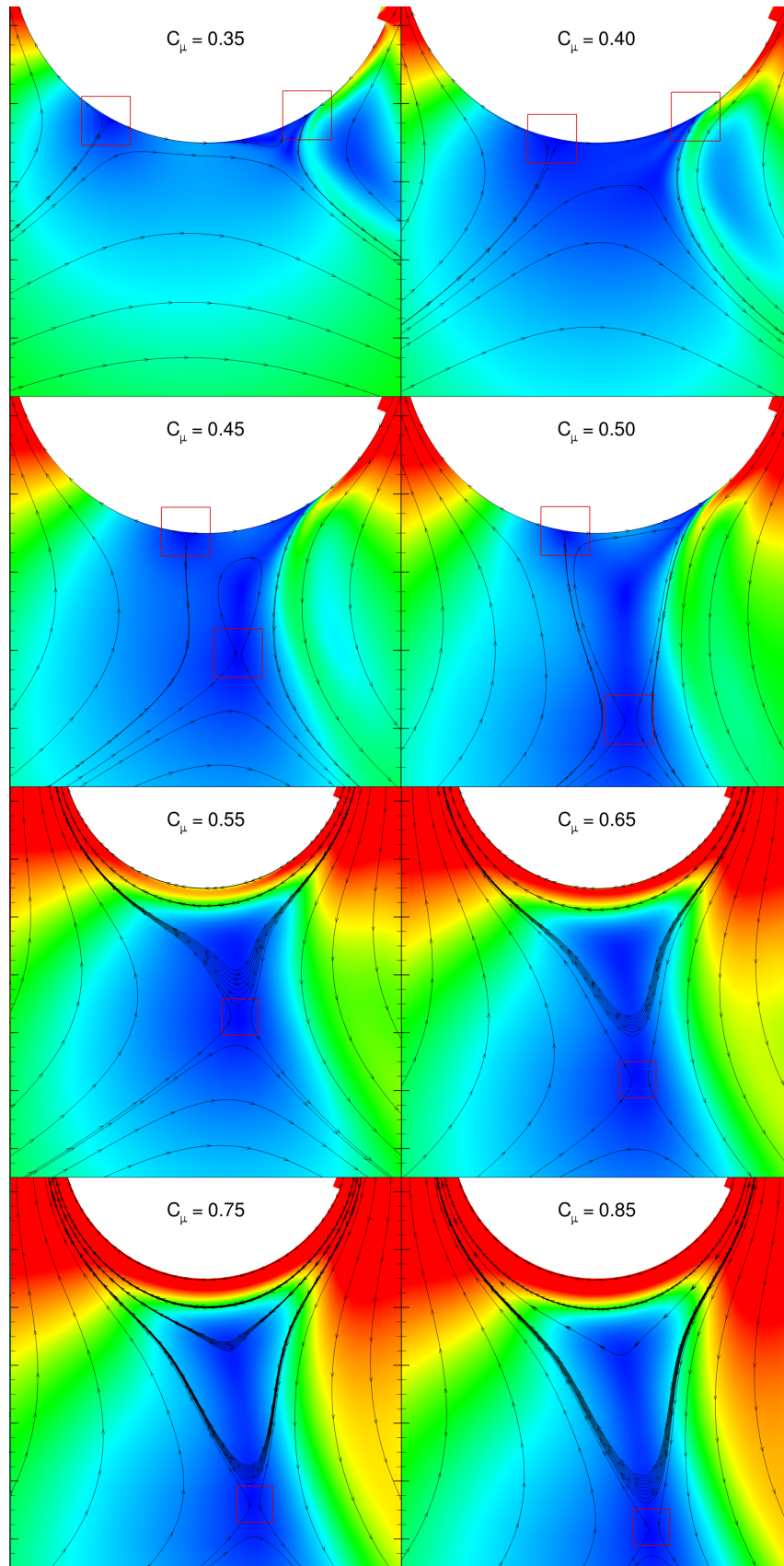


Figure 8: Mach contours and streamlines of CFJ cylinder at varying C_{μ} .

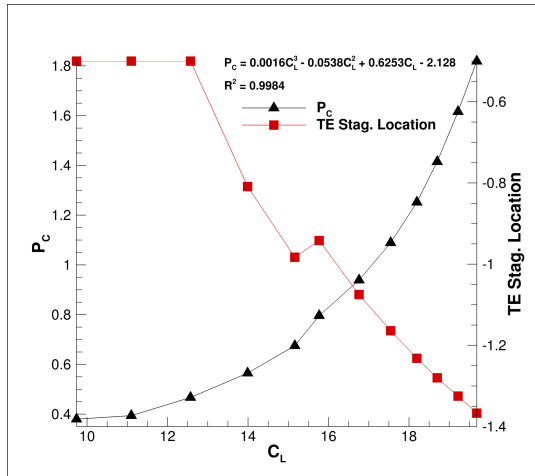


Figure 9: *CFJ cylinder power coefficient, and detached stagnation point position.*

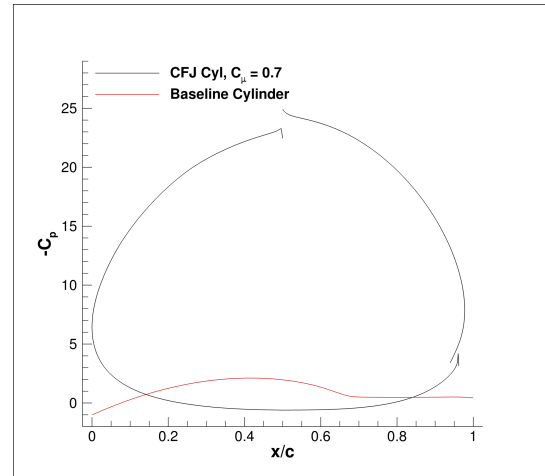


Figure 10: *CFJ cylinder C_p distribution, compared to the baseline cylinder.*

3.3 Pressure Gradients

The CFJ cylinder studied demonstrates the ability to generate substantial lift. This creates an EAPG along the top surface of the cylinder, which the CFWJ itself overcomes, maintaining attached flow on the rear of the cylinder, where the baseline cylinder would normally be separated. Fig. 10 compares the C_p distributions of the CFJ cylinder to the baseline. Fig. 12 displays the streamwise and radial pressure gradient coefficient distributions along the upper surface of the cylinders. PG_r is evaluated at a distance of 0.1% diameter away from surface of the cylinder, while PG_x is evaluated on the surface. The baseline cylinder shows a favorable streamwise pressure gradient along the leading edge until the vertical-most point on the cylinder (12 o'clock). The pressure gradient then becomes increasingly adverse, until the separation onset, indicated by the drop in PG_x , and by the drop in the surface pressure coefficient, $-C_p$.

The CFJ's streamwise favorable pressure gradient along the leading edge is several times that of the baseline cylinder's. The sudden drop in PG_x just before the top of the cylinder is caused by the injection wall jet augmenting the local favorable pressure gradient due to momentum transfer from the jet to the upstream main flow. At the topmost point the CFWJ is injected, and we observe an immensely high streamwise adverse pressure gradient $PG_x = 32.05$, about ten times that of the baseline at the top position. The APG rapidly falls off moving away from the mouth of the injection slot, but as we continue along the rear surface of the cylinder, the APG steadily climbs. The flow on the rear surface of the cylinder remains attached, and the APG reaches a magnitude about the same as the injection opening just before the rear-most point of the cylinder (3 o'clock). The streamwise APG along the wall continues to climb rapidly as the flow passes the rear-most point, into the mouth of the suction slot, where it peaks at a value of $PG_x = 53.03$.

The radial pressure gradient coefficient for both the baseline and CFJ cylinders is adverse along the entire surface. The baseline cylinder has a local maximum PG_r of 1.25 just past the cylinder LE, and a global maximum PG_r of 1.84 at the separation location. The CFJ cylinder clearly shows an EAPG rising along the leading edge, and spiking to a maximum value above $PG_r = 240$ immediately after the jet injection. The flow remains attached

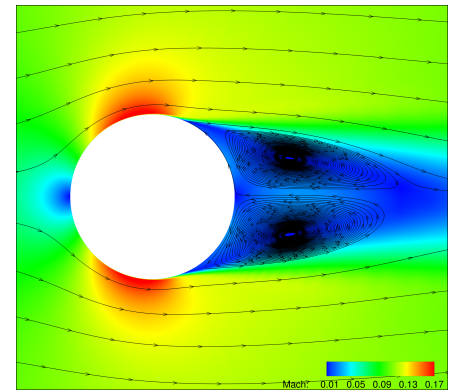


Figure 11: *Baseline cylinder Mach contour and streamlines.*

Table 2: CFJ cylinder pressure gradients

Case	C_μ	C_L	$PG_{x \max}$	$PG_{r \max}$	PGR_x	PGR_r
Baseline	-	0.000	3.2	1.84	-	-
CFJ	0.85	19.684	53	240	16.6	132

to the rear surface of the cylinder while the radial pressure gradient decreases moving towards the suction location, but remains adverse along the entire surface. The radial pressure gradient is non-zero at the leading edge of the CFJ cylinder, because there is no stagnation point at this location.

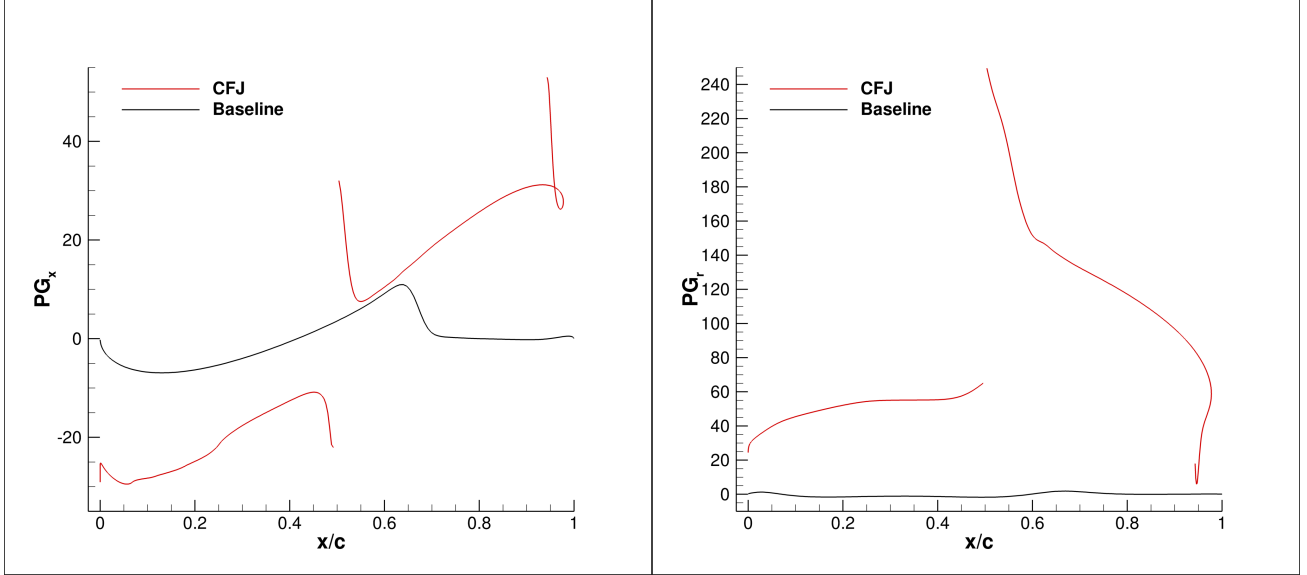


Figure 12: *Cylinder streamwise pressure gradient distribution (left), Radial pressure gradient distribution (right).*

Potential flow theory teaches us about the relation between the streamwise and radial pressure gradients. The inviscid, steady-state momentum equation for both compressible and incompressible fluids is given by:

$$(\mathbf{u} \cdot \nabla)\mathbf{u} = -\nabla p / \rho \quad (15)$$

where \mathbf{u} is the velocity magnitude. The momentum equation can be expanded to the form:

$$u \frac{\partial(u\hat{\mathbf{s}})}{\partial s} = -\frac{1}{\rho} \left(\hat{\mathbf{s}} \frac{\partial p}{\partial s} + \hat{\mathbf{r}} \frac{\partial p}{\partial r} \right) \quad (16)$$

where $\hat{\mathbf{s}}$ is a unit vector tangent to the streamline, and $\hat{\mathbf{r}}$ is an outward-pointing unit vector pointing in the direction outward from the local center of curvature of a streamline, which itself is normal to the streamline [40]. The components of fluid acceleration along the streamline and normal to the streamline are derived from the two terms in Eq. (16). The streamwise acceleration is determined by the streamwise pressure gradient as such:

$$u \frac{\partial(u)}{\partial s} = -\frac{1}{\rho} \frac{\partial p}{\partial s} \quad (17)$$

The normal component of the acceleration is a consequence of changes in the direction of the velocity. The unit vector $\hat{\mathbf{r}}$ cannot have changes in magnitude, so its changes must be in its direction. The component of the pressure gradient normal to the streamline is given by:

$$\rho \frac{u^2}{r_c} = \frac{\partial p}{\partial r} \quad (18)$$

which is the the centripetal acceleration, with r_c as the local radius of curvature. Therefore streamline curvature is associated with a component of the pressure gradient force normal to the streamlines and pointing toward the local center of curvature. Thus the radial pressure gradient is a phenomenon arising as a consequence of inviscid flow's need to turn the streamlines. The streamwise pressure gradient on the other hand is ultimately caused by changes in the velocity magnitude from viscous phenomenon like transport of energy, momentum, and shear stress.

The radius of curvature and the surface curvature are a reciprocal pair. The r_c along the outer surfaces of the CFJ cylinder is $0.5C$, and in the CFJ translation region between the injection and suction slots, it is $0.4825C$.

$$\kappa = \frac{1}{r_c} \tag{19}$$

4 Co-Flow Jet Airfoil

The CFJ and baseline airfoils are simulated at freestream Mach number of 0.03 and Reynolds number of 7.2×10^5 . A 2D CFJ airfoil has been previously investigated in [12, 13, 41, 42], and shown to possess lift coefficients far in excess of the theoretical limit dictated by Eq. (1). The CFJ6421-SST150-SUC247-INJ152 airfoil geometry used in this study is a slight modification to similar airfoils studied in the past. The injection slot is widened 30% and injection duct curvature reduced to accommodate subsonic injection flow at high C_μ and near-vertical angles of attack. This paper presents airfoil pressure gradient results at 65° AoA because of flow instability at higher AoA, regardless of injection jet strength. The CFJ mechanism is implemented via an internal pump in the same manner as the CFJ cylinder. Results of $C_\mu = 1.0 - 4.5$ are presented in Table 3. Numerical results are compared to a 2D baseline NACA6421 airfoil at the same flow conditions, but at 14° AoA (Fig. 13). It is at this AoA that the baseline NACA6421 airfoil is at its peak C_L (Fig. 14) and possesses the highest adverse pressure gradient.

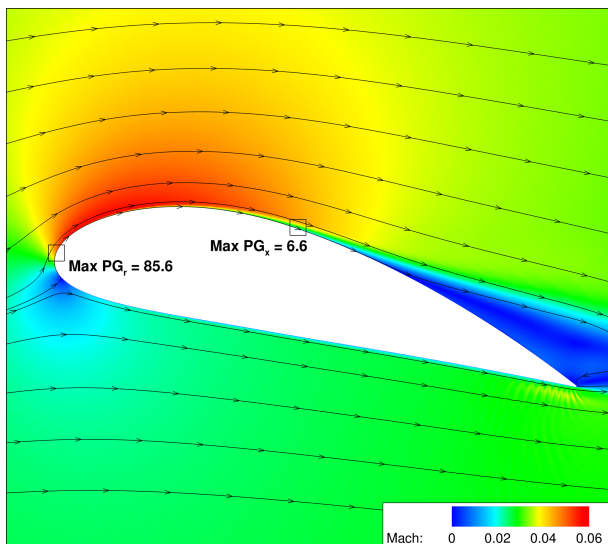


Figure 13: *Baseline 14° airfoil Mach contours.*

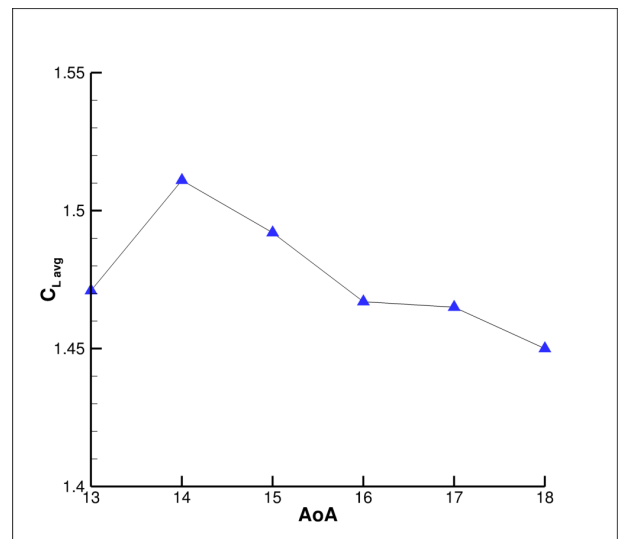


Figure 14: *Baseline airfoil C_L vs AoA.*

4.1 Mesh and Boundary Conditions

The computational domain for the 2D airfoil is normalized by the airfoil chord. A fine mesh of 365,600 cells is divided into 78 domains as shown in Fig. 15. The boundary conditions are illustrated in Fig. 16. The far-field inlet and outlet are located 200C away from the airfoil surface. The total pressure, total temperature, and flow angle are specified at the inlet boundary. Static pressure is specified at the outlet boundary. A non-slip wall BC is enforced on the walls of the airfoil and internal ducts. The CFJ iteration is implemented in the same manner as described for the cylinder in Section 3.1.

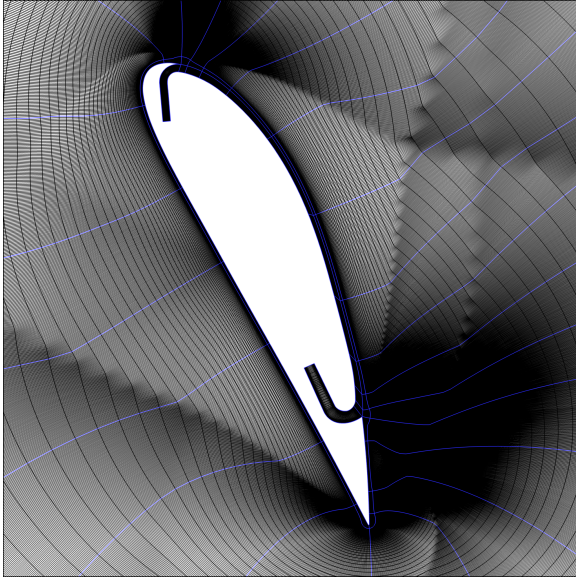


Figure 15: *CFJ6421* mesh.

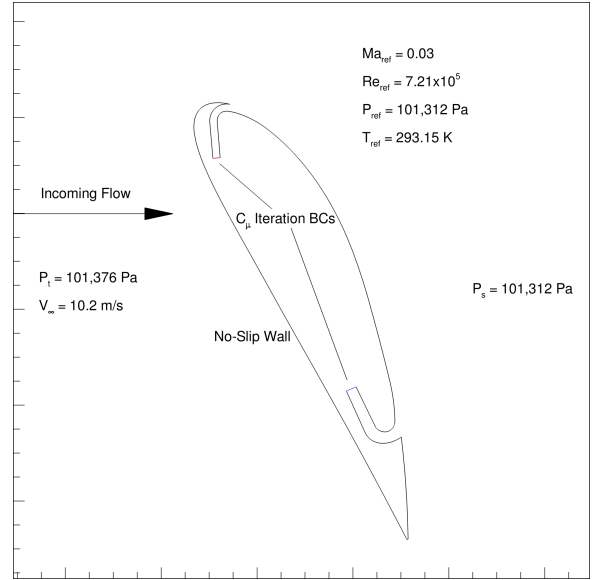


Figure 16: *CFJ6421* boundary conditions.

4.2 Flow Field

The CFJ airfoil behaves like the CFJ cylinder in many regards, but with some notable differences. Unlike the cylinder, which has a favorable pressure gradient along the LE, the airfoil studied has a severe adverse pressure gradient around the LE. Because the flow must turn sharply around features of the airfoil, we observe significantly higher pressure gradients throughout. The local radius of curvature is related to the flow angle by $1/r_c = \partial\alpha/\partial l$, so Eq. (18) can be further expanded to express the radial pressure gradient over a flow section proportional to the flow angle through which it sweeps. In this equation, α is the flow angle and l is the path length [40].

$$\frac{\partial p}{\partial r} = \rho u^2 \frac{\partial \alpha}{\partial l} \quad (20)$$

The maximum curvature at the LE of the airfoil is about $\kappa = 26.3$, or about 13.2 times greater than the curvature around the cylinder. Inside the injection duct, the turning is even sharper, reaching a curvature of $\kappa = 56.4$. The PG_r term is proportional to the curvature, thus the radial pressure gradients observed around the LE of the airfoil are much greater than those on the surface of the cylinder.

A notable difference between the flow of the CFJ airfoil and the CFJ cylinder is that the streamlines circulating the airfoil do not form a closed path near the surface like they did for the cylinder (See Figs. 4 and 5). While both LE and TE stagnation points detached from the cylinder to form a single, joined, off-body stagnation point for

the cylinder, it appears that the LE stagnation point remains on the airfoil surface even with very high injection jet power. In this situation the streamlines seem to form a cusp around the airfoil, and the LE stagnation point moves to the pressure surface of the airfoil, near the TE.

Table 3: Performance of CFJ airfoil at varying C_μ

C_μ	C_L	C_D	P_C	Γ	C_L/C_D	C_L/C_{Dc}	C_L/P_c	Inj Ma	Stag. y
1.0	6.179	0.021	0.827	1.006	294.238	7.288	7.476	0.233	Attached
1.5	8.154	0.043	1.635	1.010	189.628	4.859	4.987	0.286	Attached
2.0	10.711	-0.067	2.540	1.013	-159.866	4.332	4.218	0.336	Attached
2.5	12.561	-0.093	3.933	1.013	-135.065	3.271	3.194	0.378	Attached
3.0	13.733	-0.119	5.648	1.018	-115.403	2.484	2.431	0.414	-1.273
3.5	14.626	-0.131	7.713	1.031	-111.649	1.929	1.896	0.449	-1.390
4.0	15.315	-0.186	10.207	1.038	-82.339	1.528	1.500	0.475	-1.497
4.5	15.959	-0.181	12.860	1.045	-88.171	1.259	1.241	0.513	-1.576

Flow fields of the CFJ airfoil of $C_\mu \leq 1.5$ show minor flow instability at the rear of the airfoil, beginning at the suction slot. Flow field solutions of the CFJ airfoil show well-attached flow for $C_\mu > 1.5$. Flow along the airfoil suction surface is attached under the observed EAPG conditions. As the C_μ is increased, the LE stagnation point moves along the airfoil pressure surface towards the TE, until just before it reaches the TE point itself. Continuing to increase the C_μ , the TE stagnation point then detaches from the surface of the airfoil, while the LE stagnation point remains on the pressure surface just before the airfoil’s TE. In Table 3, the “Stag. y” column identifies the vertical distance of the detached stagnation point from the quarter-chord of the airfoil. For CFJ airfoil cases with $C_L \geq 13.73$, the TE stagnation point is detached from the surface. As the C_μ and consequently the C_L increase, the detached TE stagnation points moves farther away from the airfoil surface.

The upstream incoming flow turns to follow the contour of airfoil clockwise, turns around the LE, then stays attached to the suction surface for the length of the airfoil, as shown in Fig. 5. Due to the CFWJ flow mixing, the flow field is fully attached to the airfoil surface along the entire boundary. Fig. 17 shows that after the TE stagnation point has detached from the surface of the airfoil, as the C_μ continues to increase, the stagnation point moves down, farther away from the airfoil surface. The farther the stagnation point from the airfoil, the greater volume of freestream flow is influenced, the greater the circulation, and the greater lift the airfoil produces.

The cases studied possessing a C_μ of 1.5 and higher demonstrate a C_L exceeding Smith’s theoretical limit of 7.6, from Eq. (1). As the jet momentum coefficient C_μ increases, the C_L increases due to the lower pressure along the leading edge and suction surface translation region, and the C_D decreases because of the increasing jet momentum in the horizontal direction. The negative drag shown in Table 3 shows how the momentum from the injection jet itself creates a thrust force which is greater in magnitude than the aerodynamic drag acting on the surface of the airfoil.

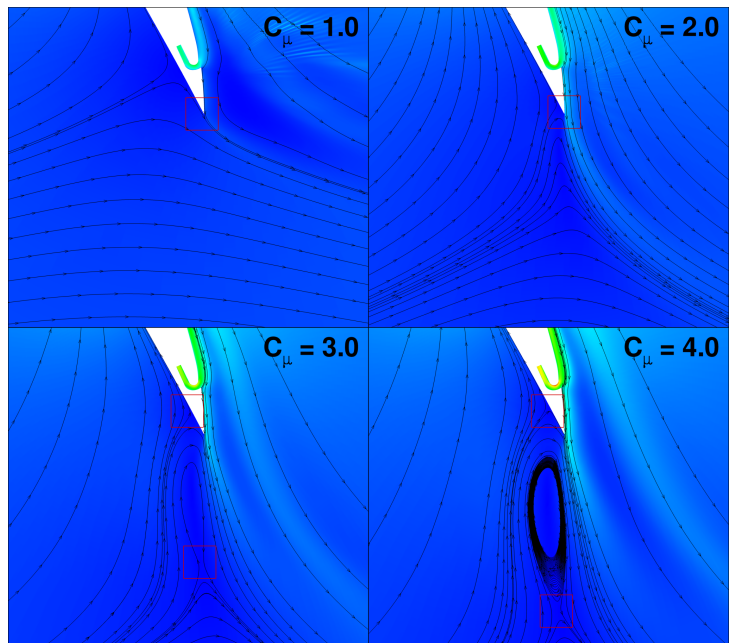


Figure 17: CFJ airfoil TE streamlines at varying C_μ .

4.3 Pressure Gradients

Fig. 18 shows the computed airfoil surface pressure coefficient $-C_p$ for the baseline airfoil at 14° AoA and the CFJ airfoil profile at 65° AoA and $C_\mu = 4.5$. The baseline airfoil has a suction peak $-C_p$ of almost 3, whereas the CFJ-NACA6421 airfoil's peak value is close to 140. The CFJ airfoil creates an EAPG $PG_x \approx 1792$ at about the same location as the C_p peak past the leading edge, which is about 270 times higher than that of the baseline.

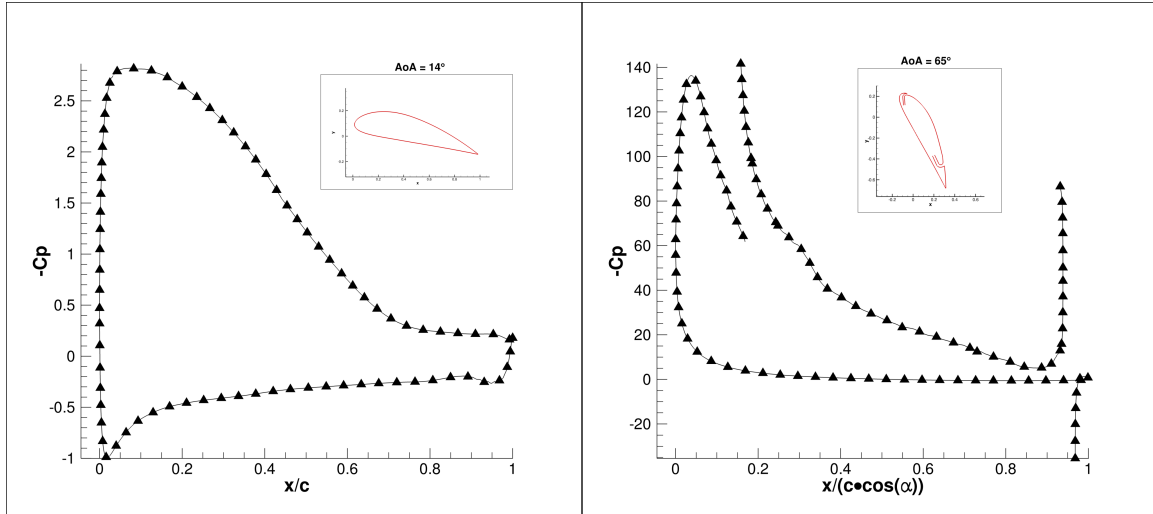


Figure 18: C_p distribution: Baseline NACA6421 airfoil at $AoA=14^\circ$ (left), CFJ airfoil at $AoA=65^\circ$, $C_\mu = 0.45$ (right).

The streamlines transit around the leading edge by nearly 180° as shown in Fig. 5. The leading edge peak Mach number reaches 0.345, 11.5 times higher than the freestream Mach number as shown in Fig. 5 (upper left). It generates a “super-suction” effect at the LE which contributes to the high lift coefficient and thrust generation shown in Fig. 3. For the cases studied in this paper, the maximum streamwise pressure gradient PG_x at the leading edge of the airfoil is roughly 270 times the magnitude of the maximum PG_x for the baseline airfoil at its max C_L condition, and the maximum centrifugal pressure gradient PG_r measured is roughly 68 times that of the baseline. Such a high resilience to the extreme adverse centrifugal pressure gradient without detaching the flow must be attributed to the induction effect of the CFWJ injection located downstream.

The CFJ6421 airfoil studied shows the ability to add significant circulation to the flow field, generating lift far beyond the limit set in Eq. (1). This creates an EAPG around the LE of the airfoil and down the length of the suction surface transition. The CFJ airfoil overcomes extreme adverse pressure gradients to maintain attached flow along its entire suction surface for angles of attack far beyond what a baseline airfoil could manage. Fig. 19 shows that at the very leading edge of the airfoil, the flow experiences a favorable streamwise pressure gradient coefficient PG_x , but it quickly rises to an adverse pressure gradient past the LE, to a peak value of 1792. The baseline NACA6421 airfoil at 14° displays a maximum PG_x past the LE of just 6.6. The EAPG declines somewhat approaching the injection slot. Like the CFJ cylinder, the maximum streamwise pressure gradient coefficient PG_x is observed at the location of the injection jet, with a computed magnitude of $PG_x = 7200$. The EAPG declines rapidly away from the injection slot, but maintains a magnitude qualifying it as an EAPG along the entire length of the suction surface transition region. The PG_r distribution is similar to the PG_x distribution. The radial adverse pressure gradient increases in strength as the flow moves towards the LE, and decreases in strength past the leading edge, peaking at 5850. The baseline NACA6421 sees a maximum PG_r of just 85.6. Like the cylinder, the maximum PG_r for the CFJ airfoil is measured directly after the injection slot, with a value of 10380. The pressure field and positions of each maximum pressure gradient coefficient are labelled in Fig. 20.

Table 4: CFJ airfoil pressure gradients

Case	C_μ	C_L	$PG_x LE$	$PG_r LE$	$PG_x inj$	$PG_r inj$	PGR_x	PGR_r
Baseline	-	1.511	6.6	85.6	-	-	-	-
CFJ	4.5	15.959	1792	5850	7200	10380	1091	121

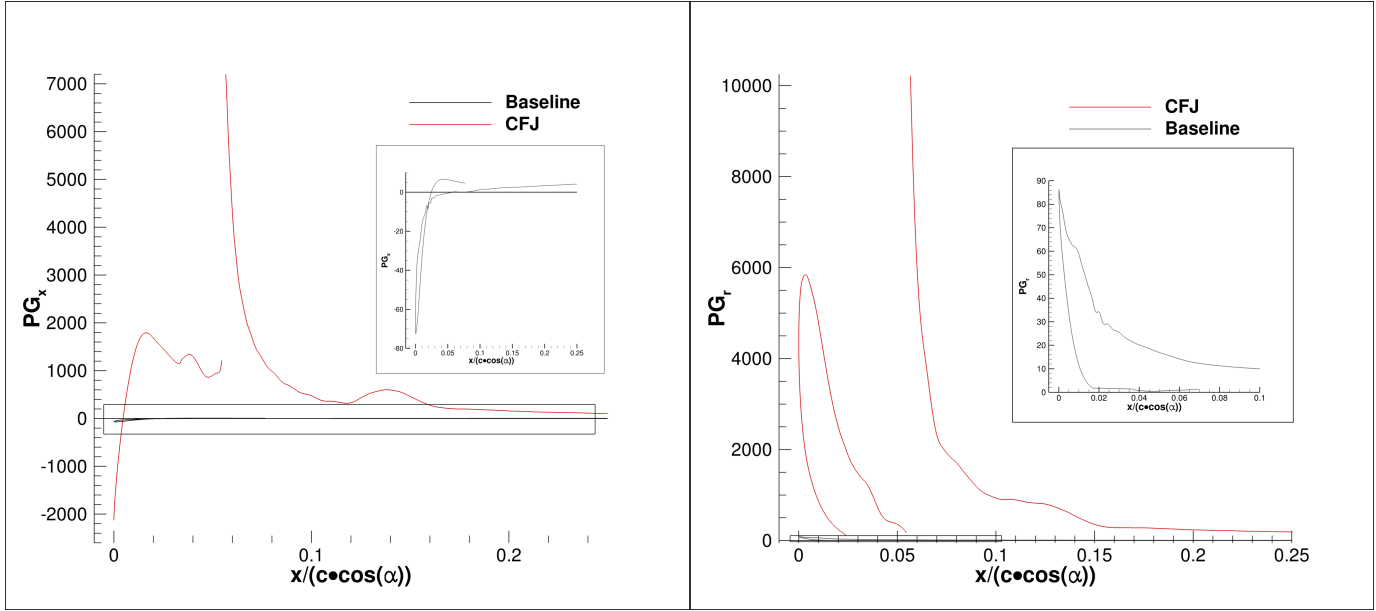


Figure 19: *Cylinder streamwise pressure gradient distribution (left), Radial pressure gradient distribution (right).*

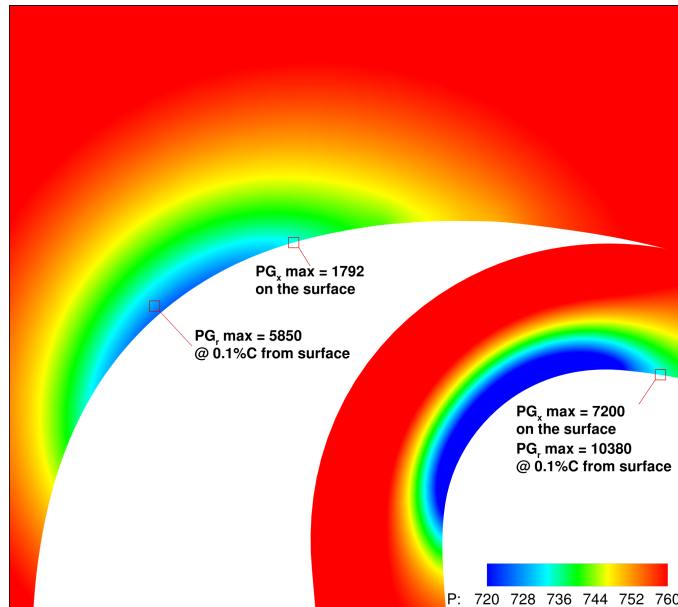


Figure 20: *CFJ maximum pressure gradient locations and pressure field.*

5 Conclusions

This paper presents a 2D numerical analysis of a CFJ cylinder and a CFJ-NACA6421 airfoil at Mach number 0.1 and 0.03 respectively, which create and maintain adverse pressure gradients of magnitudes far beyond those observed for non-flow-controlled airfoils. According to conventional knowledge, these bodies should not be able to generate lift. However, the implementation of the co-flow jet onto these two bodies allows them to maintain flow attachment and generate lift despite being subjected to adverse pressure gradients which should detach the flow from the suction surface. The process by which the CFJ generates lift – by creating an EAPG along the top surface and maintaining attached flow in that EAPG – seems to be unique in the field of flow control. Maintaining attached flow in the presence of a pressure gradient at least ten times that which would normally lead to separation provides the means by which these bodies generate lift coefficients up to magnitudes in excess of the airfoil lift limit established by Smith [21].

The CFJ demonstrates the capability to attach the jet flow to the upper surface of the airfoil, and also to attach the incoming flow to the leading edge of the airfoil, despite the presence of an extreme adverse pressure gradient which would typically lead to separated flow. The CFJ transfers momentum and energy from the jet to the freestream flow, greatly increasing the circulation around the CFJ cylinder and CFJ airfoil. For both the CFJ cylinder and airfoil cases, the LE and TE stagnation points move along the surface towards the bottom-most point as the circulation increases. Once the circulation exceeds a critical value, at least one stagnation point detaches from the surface, forming a virtual extension of the lifting surface. The lift coefficients measured for the CFJ cylinder and CFJ airfoil far exceed their baseline counterparts, showing lift coefficients up to 19.68 and 15.96.

An EAPG is defined to be an adverse pressure gradient of at least one order of magnitude greater than that which could be sustained by the non-controlled flow of a baseline case. The CFJ cylinder cases studied show the radial extreme adverse pressure gradient to be 16.6 times the baseline cylinder APG, and 132 times the baseline's streamwise APG. The CFJ airfoil shows 121 times the baseline airfoil for the radial EAPG, and 1091 times the baseline for the streamwise EAPG. While both the CFJ cylinder and CFJ airfoil demonstrate the ability to create an EAPG, the magnitudes of the pressure gradients seen in the CFJ airfoil cases far exceed those of the CFJ cylinder cases, because the CFJ airfoil forces the flow to turn much more rapidly. The curvature of the CFJ airfoil at both the leading edge and for the CFJ injection duct is much higher than that of the the cylinder surface, explaining the greatly increased centripetal acceleration and corresponding radial pressure gradient.

For CFJ cylinder cases with $C_L \geq 13.99$, at least one stagnation point has detached from the surface. At $C_L \geq 15.77$, both LE and TE stagnation points are detached. For CFJ airfoil cases with $C_L \geq 13.73$, the TE stagnation point detaches from the surface, and continues to move farther away from the airfoil surface as the C_μ and the C_L increase. In both cases, the stagnation point detachment occurs while the C_L exceeds the theoretical airfoil lift limit established by Smith in Eq. (1).

The streamwise and radial pressure gradients are related by a fluid particle's acceleration along a streamline. The radial pressure gradient arises as a consequence of streamline turning, which is an inviscid effect provided the flow is attached. The streamwise pressure gradient is ultimately caused by acceleration along a streamline due to viscous phenomenon like transport of energy, momentum, and shear stress.

Due to its ability to maintain attached flow in the presence of an EAPG, the CFJ presents an efficient and compact method of flow control with the potential to be far more effective than other active flow control devices. The existence, magnitude, and causes of the EAPG enabled by the CFJ merits further study, and should be verified via wind tunnel experimentation. Additionally, the Spalart-Allmaras turbulence model [26] may not be suited to properly resolving flow attachment along the wall in the presence of such a significant pressure gradient, and the flow attachment should be evaluated using a higher accuracy model like LES or DNS.

6 Acknowledgements

The simulations are conducted on Pegasus super-computing system at the Center for Computational Sciences at the University of Miami.

Disclosure: The University of Miami and Dr. Gecheng Zha may receive royalties for future commercialization of the intellectual property used in this study. The University of Miami is also equity owner in CoFlow Jet, LLC, licensee of the intellectual property used in this study.

References

- [1] Zha, G.-C. and Gao, W. and Paxton, C., “Jet Effects on Co-Flow Jet Airfoil Performance,” *AIAA Journal*, No. 6,, vol. 45, pp. 1222–1231, 2007.
- [2] G.-C. Zha and D. C. Paxton, “A Novel Flow Control Method for Airfoil Performance Enhancement Using Co-Flow Jet.” *Applications of Circulation Control Technologies*, Chapter 10, p. 293-314, Vol. 214, Progress in Astronautics and Aeronautics, AIAA Book Series, Editors: Joslin, R. D. and Jones, G.S., 2006.
- [3] Zha, G.-C and Paxton, C. and Conley, A. and Wells, A. and Carroll, B., “Effect of Injection Slot Size on High Performance Co-Flow Jet Airfoil,” *AIAA Journal of Aircraft*, vol. 43, 2006.
- [4] Zha, G.-C and Carroll, B. and Paxton, C. and Conley, A. and Wells, A., “High Performance Airfoil with Co-Flow Jet Flow Control,” *AIAA Journal*, vol. 45, 2007.
- [5] Wang, B.-Y. and Haddoukessouni, B. and Levy, J. and Zha, G.-C., “Numerical Investigations of Injection Slot Size Effect on the Performance of Co-Flow Jet Airfoil ,” *AIAA Journal of Aircraft*, vol. 45, pp. 2084–2091, 2008.
- [6] B. P. E. Dano, D. Kirk, and G.-C. Zha, “Experimental Investigation of Jet Mixing Mechanism of Co- Flow Jet Airfoil.” AIAA-2010-4421, (5th AIAA Flow Control Conference, Chicago, IL), 28 Jun - 1 Jul 2010.
- [7] B. P. E. Dano, G.-C. Zha, and M. Castillo, “Experimental Study of Co-Flow Jet Airfoil Performance Enhancement Using Micro Discreet Jets.” AIAA Paper 2011-0941, 49th AIAA Aerospace Sciences Meeting, Orlando, FL,, 4-7 January 2011.
- [8] Lefebvre, A. and Dano, B. and Bartow, W. and Di Franzo, M. and Zha, G.-C., “Performance and Energy Expenditure of Co-Flow Jet Airfoil with Variation of Mach Number,” *AIAA Journal of Aircraft*, vol. 53, pp. 1757–1767, 2016.
- [9] Wang, B. Y and Zha, G.-C., “ Detached-Eddy Simulation of a Co-Flow Jet Airfoil at High Angle of Attack ,” *AIAA Journal of Aircraft*, vol. 48, pp. 1495–1502, 2011.
- [10] Im, H.-S. and Zha, G.-C. and Dano, B. P. E., “Large Eddy Simulation of Coflow Jet Airfoil at High Angle of Attack,” *Journal of Fluid Engineering*, vol. 136(2), p. 021101, 2014.
- [11] Lefebvre, A. and Zha, G.-C., “Trade Study of 3D Co-Flow Jet Wing for Cruise and Takeoff/Landing Performance.” AIAA Paper 2016-0570, AIAA SCITECH2016, AIAA Aerospace Science Meeting, San Diego, CA, 4-8 January 2016.

- [12] Yang, Y.-C. and Zha, G.-C., “Super-Lift Coefficient of Active Flow Control Airfoil: What Is the Limit?.” AIAA Paper 2017-1693, AIAA SCITECH2017, 55th AIAA Aerospace Science Meeting, Grapevine, Texas, 9-13 January 2017.
- [13] G.-C. Zha, Y.-C. Yang, Y. Ren, and B. McBreen, “Super-lift and thrusting airfoil of coflow jet-actuated by micro-compressors.” AIAA Paper 2018-3061, AIAA AVIATION 2018, Atlanta, GA , 25 - 29 June 2018.
- [14] K. Xu and G. Zha, “Investigation of coflow jet active flow control for wind turbine airfoil.” AIAA 2020-2942, 2020 AIAA AVIATION Forum and Exposition, Virtual Event, 15-19 June, 2020.
- [15] K.-W. Xu and G.-C. Zha, “High control authority 3d aircraft control surfaces using co-flow jet,” *AIAA Journal of Aircraft*, July 2020.
- [16] K.-W. Xu, Y. Ren, and G.-C. Zha, “Flow separation control by coflow wall jet.” AIAA Paper 2021-2946, AIAA Aviation 2021, 2-6 Aug. 2021.
- [17] K.-W. Xu, B. McBreen, Y. Ren, and G.-C. Zha, “Analysis of Micro-compressor Performance with Integrated Co-flow Jet Airfoil Ducting System .” AIAA Paper 2020-0047, 2020 AIAA SciTech Forum, Orlando, FL, 6-10 January, 2020.
- [18] Kewei Xu, Gecheng Zha.
- [19] Kewei Xu, Yan Ren, Gecheng Zha.
- [20] G.-C. Zha, “ESTOL Performance for Heavy Lift Transports Using Ultra-High Lift High Efficiency Co-Flow Jet Airfoil.” Final Report to DARPA for Contract HR0011-16-2-0052, May 25, 2018.
- [21] A. Smith, “High-Lift Aerodynamics,” *Journal of Aircraft*, vol. 12, pp. 501–530, 1975.
- [22] T. O. G. Prandtl, Ludwig, *Applied Hydro- and Aeromechanics (Dover Books on Aeronautical Engineering)*. Dover Publications, 1934.
- [23] V. E. Lockwood, “Lift generation on a circular cylinder by tangential blowing from surface slots.” NASA TN D-244, May 1960.
- [24] P. Tokumaru and P. Dimotakis, “The lift of a cylinder executing rotary motions in a uniform flow,” *Journal of Fluid Mechanics*, vol. 255, pp. 1–10, 1993.
- [25] Yang, Y.-C. and Zha, G.-C., “Super Lift Coefficient of Cylinder Using Co-Flow Jet Active Flow Control.” AIAA Paper 2018-0329, AIAA SciTech Forum, 2018 AIAA Aerospace Sciences Meeting, Kissimmee, FL, 8-12 January 2018.
- [26] P. Spalart and S. Allmaras, “A One-equation Turbulence Model for Aerodynamic Flows.” AIAA-92-0439, 1992.
- [27] B. E. Launder and W. Rodi, “The Turbulent Wall Jet - Measurement and Modeling,” *Journal of Fluid Mechanics*, vol. 15, pp. 429–59, 1983.
- [28] H. P. A. H. Irwin, “Measurement in a self-preserving plane wall jet in a positive pressure gradient,” *Journal of Fluid Mechanics*, vol. 61, pp. 33–63, 1973.
- [29] George, W. K. and Abrahamsson, H. and Eriksson, J. and Karlsson, R. I. and Löfdahl, L. and Wosnik, M. , “A similarity theory for the turbulent plane wall jet without external stream ,” *J. Fluid Mech.*, vol. 425, 2000.

- [30] Dejoan, A. and Leschziner, M. A. , “Large eddy simulation of a plane turbulent wall jet,” *PHYSICS OF FLUIDS*, vol. 17, 2005.
- [31] Wang, B.Y., and Zha, G.C., “ Detached Eddy Simulations of a Circular Cylinder Using a Low Diffusion E-CUSP and High-Order WENO Scheme.” AIAA Paper 2008-3855, AIAA 38th Fluid Dynamics Conference, Seattle, Washington, June 23-26, 2008.
- [32] Shen, Y.Q., Zha, G.C., and Wang, B.Y., “Improvement of Stability and Accuracy of Implicit WENO Scheme,” *AIAA Journal*, vol. 47, pp. 331–334, DOI:10.2514/1.37697, 2009.
- [33] Shen, Y.Q., and Zha, G.C., “Improvement of the WENO Scheme Smoothness Estimator,” *International Journal for Numerical Methods in Fluids*, vol. 64., pp. 653–675, DOI:10.1002/flid.2186, 2009.
- [34] Shen, Y.Q., Wang, B.Y., and Zha, G.C., “Implicit WENO Scheme and High Order Viscous Formulas for Compressible Flows .” AIAA Paper 2007-4431, 2007.
- [35] Shen, Y.Q., Zha, G.C., and Chen, X., “High Order Conservative Differencing for Viscous Terms and the Application to Vortex-Induced Vibration Flows,” *Journal of Computational Physics*, vol. 228(2), pp. 8283–8300, doi:10.1016/j.jcp.2009.08.004, 2009.
- [36] Shen, Y.Q., and Zha, G.C., “Large Eddy Simulation Using a New Set of Sixth Order Schemes for Compressible Viscous Terms,” *Journal of Computational Physics*, vol. 229, pp. 8296–8312, doi:10.1016/j.jcp.2010.07.017, 2010.
- [37] Zha, G.C., Shen, Y.Q. and Wang, B.Y., “An improved low diffusion E-CUSP upwind scheme ,” *Journal of Computer and Fluids*, vol. 48, pp. 214–220, Sep. 2011.
- [38] G.-C. Zha and E. Bilgen, “Numerical Study of Three-Dimensional Transonic Flows Using Unfactored Upwind-Relaxation Sweeping Algorithm,” *Journal of Computational Physics*, vol. 125, pp. 425–433, 1996.
- [39] B.-Y. Wang and G.-C. Zha, “A General Sub-Domain Boundary Mapping Procedure For Structured Grid CFD Parallel Computation,” *AIAA Journal of Aerospace Computing, Information, and Communication*, vol. 5, No.11, pp. 2084–2091, 2008.
- [40] E. M. Greitzer, C. S. Tan, and M. B. Graf, *Internal Flow*. Cambridge University Press, 2004.
- [41] Y. Wang and G.-C. Zha, “Study of Mach Number Effect for 2D Co-Flow Jet Airfoil at Cruise Conditions.” AIAA Paper 2019-3169, AIAA Aviation 2019, AIAA Applied Aerodynamics Conference, Dallas, Texas, 17-21 June 2019.
- [42] Y. Wang, Y.-C. Yang, and G.-C. Zha, “Study of Super-Lift Coefficient of Co-Flow Jet Airfoil and Its Power Consumption.” AIAA Paper 2019-3652, AIAA Aviation 2019, AIAA Applied Aerodynamics Conference, Dallas, Texas, 17-21 June 2019.